Inverse Mass Matrix via the Method of Localized Lagrange Multipliers

José A. González[1], R. Kolman[2], S.S. Cho[3], C. A. Felippa[4], K.C. Park[4],[*]

[1]*Escuela Técnica Superior de Ingeniería, Universidad de Sevilla,*
Camino de los Descubrimientos s/n, Seville E-41092, Spain.
[2]*Institute of Thermomechanics, The Czech Academy of Sciences,*
Dolejškova 5, 182 00 Prague, Czech Republic.
[3]*Reactor Mechanical Engineering Division, Korea Atomic Energy Research Institute,*
999-111 Daedeok-Daero, Yuseong-gu, Daejeon 305-353, Republic of Korea.
[4]*Department of Aerospace Engineering Sciences, University of Colorado at Boulder, CO 80309-429, USA.*

SUMMARY

An efficient method for generating the mass matrix inverse of structural dynamic problems is presented, which can be tailored to improve the accuracy of target frequency ranges and/or wave contents. The present method bypasses the use of biorthogonal construction of a kernel inverse mass matrix that requires special procedures for boundary conditions and free edges or surfaces, and constructs the free-free inverse mass matrix employing the standard FEM procedure. The various boundary conditions are realized by the the method of localized Lagrange multipliers. In particular, the present paper constructs the kernel inverse matrix by employing the standard FEM elemental mass matrices. It is shown that the accuracy of the present inverse mass matrix is almost identical to that of a conventional consistent mass matrix or a combination of lumped and consistent mass matrices. Numerical experiments with the proposed inverse mass matrix are carried out to validate its effectiveness when applied to vibration analysis of bars, beams and plain stress problems. Copyright © 2017 John Wiley & Sons, Ltd.

1. INTRODUCTION

Recently, improvements of FEM mass matrices have been receiving an intense attention in the computational mechanics community [1, 2, 3, 4, 5]. The need for mass matrix improvements come from two distinct motivations: efficient large explicit time integration step lengths for the analysis of highly nonlinear transient structural dynamics and dispersion accuracy improvements for wave propagation analysis [6, 7, 8, 9, 10]. The first one has been addressed by adopting lumped mass matrices that improves computational efficiency and at the same time decreases the highest frequency (often equalling to the highest mesh frequency). The second need arises from the requirements of high accuracy in the transmitting forces with high-frequency stress waves. This is where a diagonalized mass matrix may not yield sufficiently accurate results, hence the search for non-diagonal mass matrix continues to date.

Ideally, an inverse mass matrix should possess the following properties:

---

[*]Correspondence to: K.C. Park, Department of Aerospace Engineering Sciences, University of Colorado, Boulder, CO 80309-429, USA. E-mail: kcpark@colorado.edu

1. It should accurately capture both low and intermediate-frequency response components.
2. Except for discontinuous wave propagation problems, its numerically stable explicit integration step size should be much larger than employing the standard mass matrix.
3. Its inverse should be inexpensive to generate, preferably without factorization computations.

Recently, Tkachuk and Bischoff [5] presented an innovative method for constructing an inverse mass matrix based on Hamilton's principle with momentum and displacement $(\boldsymbol{p}, \boldsymbol{u})$ variables. A key idea in their work is the discretization of the momentum-based kinetic energy in terms of a set of biorthogonal basis functions corresponding to the displacement basis functions. The method proposed in [5] resorts to non-standard finite element construction with special tailoring for treating the Dirichlet boundary terms. Hence, considerable modifications of the existing finite element software modules are required. When one contemplates element-by-element construction of the inverse of the global mass matrix, many degrees of freedom belong to the cross points and boundary nodes, which implies that one has to replace the existing mass matrix routines by specially constructed mass matrix inverse.

The present method, while employing the same momentum-velocity formulation as adopted in [5] only as a formulation vehicle, utilizes standard FEM procedures, thus alleviates the special treatments associated the use of biorthogonal construction and mass matrix modification via a penalty procedure. Specifically, we outline the present method as follows:

First, we abandon the biorthogonal generation of the elemental kernel inverse mass matrix. Instead, we utilize the standard FEM mass matrix with a diagonalized mass-like matrix to construct the elemental kernel inverse matrix.

Second, the present proposed method does not require the penalty insertion to improve the accuracy of the procedure presented in [5]. It is shown that the accuracy of the present method is almost identical to that of a weighted elemental mass matrix of a lumped and consistent elemental mass matrix.

Third, boundary conditions are enforced by the method of localized Lagrange multipliers [11, 12, 13, 14], hence the present method needs only free-free inverse matrices. This makes the present method applicable to all the existing element types. Since the number of boundary degrees of freedom is usually substantially smaller than the those of the resulting size of the unknown equations, the cost associated with the enforcement of the boundary conditions via the localized method of Lagrange multipliers is insignificant as will be shown subsequently.

The paper is organized as follows. Section 2 derives from Hamilton's principle the $(\mathbf{p}, \mathbf{u})$ mixed equations of elastodynamics and describes the direct construction of inverse mass matrices through biorthogonal basis functions. The incorporation of boundary conditions into the inverse mass matrix is described in Section 3, together with its mathematical formalization through the use of a projector. Furthermore, a new method for selective mass scaling that reduces the maximum frequencies is described in Section 4. In Section 5, a series of numerical examples are solved and compared with analytical solutions to demonstrate the accuracy of the proposed methodology. Finally, Section 6 closes with some concluding remarks.

2. BASIS FOR CONSTRUCTING INVERSE MASS MATRIX VIA THE LOCALIZED LAGRANGE MULTIPLIERS

The prevailing practice for computing the mass matrix $\mathbf{M}$ in the finite element method is to use a bilinear form of the system kinetic energy T, viz.,

$$T = \int_{\Omega} \tfrac{1}{2} \rho \boldsymbol{v}(\mathbf{x}, t) \cdot \boldsymbol{v}(\mathbf{x}, t) \, d\Omega \approx \tfrac{1}{2} \dot{\mathbf{u}}(t)^{\mathsf{T}} \mathbf{M} \, \dot{\mathbf{u}}(t) \tag{1}$$

where $\boldsymbol{v}(\mathbf{x}, t)$ and $\dot{\mathbf{u}}(t)$ are the continuum velocity and discrete approximate velocity, respectively. Since our objective is to generate the inverse mass matrix directly, instead of employing matrix

inversion, we employ a dual form of the kinetic energy:

$$T = \int_\Omega \frac{1}{2\rho} \boldsymbol{p}(\mathbf{x}, t) \cdot \boldsymbol{p}(\mathbf{x}, t) \, d\Omega \approx \frac{1}{2} \mathbf{p}(t)^\mathsf{T} \mathbf{C} \mathbf{p}(t) \tag{2}$$

where $\boldsymbol{p}(\mathbf{x}, t)$ and $\mathbf{p}(t)$ are respectively the continuum and discrete approximate momentum vectors, and $\mathbf{C}$ is defined as the Reciprocal Mass Matrix (RMM).

It will be shown that an inverse of the mass matrix can be obtained via:

$$\mathbf{M}^{-1} = \mathbf{A}^{-\mathsf{T}} \mathbf{C} \mathbf{A}^{-1} \tag{3}$$

where $\mathbf{A}$ is the dual-base projection matrix, that can be transformed into a diagonal area/volume-like matrix. Hence, the computational simplicity of obtaining an inverse of the mass matrix via this new route.

To this end, we invoke Hamilton's principle for constrained elastodynamic problems. This principle states that *the path followed by a dynamic system is the one which minimizes the action integral of the Lagrangian*; condition that can be expressed using the following three-field variational form:

$$\delta H(\boldsymbol{u}, \boldsymbol{p}, \boldsymbol{\ell}) = \int_{t_1}^{t_2} \delta \left\{ T(\dot{\boldsymbol{u}}, \boldsymbol{p}) - U(\boldsymbol{u}, \boldsymbol{\ell}) + W(\boldsymbol{u}) \right\} \, dt = 0 \tag{4}$$

were δT is the virtual kinetic energy, δU the virtual elastic energy and δW the virtual work done by the external loads, magnitudes that can be expressed:

$$\delta T = \int_\Omega \delta(\tfrac{1}{2} \boldsymbol{p} \cdot \dot{\boldsymbol{u}}) \, d\Omega \tag{5}$$

$$\delta U = \int_\Omega \delta \boldsymbol{\varepsilon} : \boldsymbol{\sigma} \, d\Omega + \int_\Gamma \delta \left\{ \boldsymbol{\ell} \cdot (\boldsymbol{u} - \boldsymbol{u}_b) \right\} \, d\Gamma \tag{6}$$

$$\delta W = \int_\Omega \delta \boldsymbol{u} \cdot \boldsymbol{f} \, d\Omega \tag{7}$$

with known displacement boundary conditions $\boldsymbol{u}_b$ imposed at interface Γ by using a field of localized Lagrange multipliers $\boldsymbol{\ell}$ and external body forces per unit volume $\boldsymbol{f}$ acting on Ω.

By making use of the momentum-velocity relation ($\boldsymbol{p} = \rho \dot{\boldsymbol{u}}$) in the following identity:

$$\tfrac{1}{2} \boldsymbol{p} \cdot \dot{\boldsymbol{u}} = \boldsymbol{p} \cdot \dot{\boldsymbol{u}} - \tfrac{1}{2\rho} \boldsymbol{p} \cdot \boldsymbol{p} \tag{8}$$

we can obtain an equivalent expression for the virtual kinetic energy per unit volume:

$$\delta \left(\tfrac{1}{2} \boldsymbol{p} \cdot \dot{\boldsymbol{u}} \right) = \delta \dot{\boldsymbol{u}} \cdot \boldsymbol{p} + \delta \boldsymbol{p} \cdot \left(\dot{\boldsymbol{u}} - \tfrac{1}{\rho} \boldsymbol{p} \right) \tag{9}$$

and finally performing an integration by parts of the second term of the last equation yields:

$$\int_{t_1}^{t_2} \delta \dot{\mathbf{u}} \cdot \boldsymbol{p} \, dt = - \int_{t_1}^{t_2} \delta \boldsymbol{u} \cdot \dot{\boldsymbol{p}} \, dt \tag{10}$$

relation that can be used to eliminate the virtual velocity field from the formulation.

Introducing previous identities, (9) and (10), into the principle of stationary action (4), we obtain the final the three-field variational form of the Hamilton's principle for constrained elastodynamics:

$$\delta H(\boldsymbol{u}, \boldsymbol{p}, \boldsymbol{\ell}) = \int_{t_1}^{t_2} \left\{ \int_\Omega \delta \boldsymbol{p} \cdot \left(\dot{\boldsymbol{u}} - \tfrac{1}{\rho} \boldsymbol{p} \right) d\Omega - \int_\Omega \left(\delta \boldsymbol{u} \cdot \dot{\boldsymbol{p}} + \delta \boldsymbol{\varepsilon} : \boldsymbol{\sigma} \right) d\Omega + \int_\Omega \delta \boldsymbol{u} \cdot \boldsymbol{f} \, d\Omega \right.$$
$$\left. + \int_\Gamma \delta \boldsymbol{u} \cdot \boldsymbol{\ell} \, d\Gamma - \int_\Gamma \delta \boldsymbol{\ell} \cdot (\boldsymbol{u} - \boldsymbol{u}_b) \, d\Gamma \right\} dt = 0 \quad (11)$$

expression that will be used to derive the equations of motion.

Discretization in space of this mixed form is performed by using independent shape functions for displacements, momenta and Lagrangian multipliers. We carry out then a standard mixed FEM discretization with independent shape functions for the three fields:

$$\boldsymbol{u} = \mathbf{N}_u \mathbf{u}, \qquad \boldsymbol{p} = \mathbf{N}_p \mathbf{p}, \qquad \boldsymbol{\ell} = \mathbf{N}_\lambda \boldsymbol{\lambda} \tag{12}$$

and introducing these approximations in (11) one obtains the following set of semi-discrete equations:

$$\mathbf{A}^\mathsf{T} \dot{\mathbf{u}} - \mathbf{C}\mathbf{p} = \mathbf{0} \qquad \text{\textit{Momentum equation}} \tag{13}$$

$$\mathbf{A}\dot{\mathbf{p}} + \mathbf{B}\boldsymbol{\lambda} = \mathbf{r} \qquad \text{\textit{Equilibrium equation}} \tag{14}$$

$$\mathbf{B}^\mathsf{T}\mathbf{u} - \mathbf{L}_b \mathbf{u}_b = \mathbf{0} \qquad \text{\textit{Boundary (and interface) constraints}} \tag{15}$$

$$-\mathbf{L}_b^\mathsf{T}\boldsymbol{\lambda} = \mathbf{0} \qquad \text{\textit{Newton's 3rd law on the boundaries}} \tag{16}$$

where vector $\mathbf{r} = \mathbf{f} - \mathbf{f}^{int}$ is the external-internal forces residual and the matrix components are expressed:

$$\mathbf{A} = \int_\Omega \mathbf{N}_u^\mathsf{T} \, \mathbf{N}_p \, d\Omega \tag{17}$$

$$\mathbf{C} = \int_\Omega \tfrac{1}{\rho} \mathbf{N}_p^\mathsf{T} \, \mathbf{N}_p \, d\Omega \tag{18}$$

$$\mathbf{B} = \int_\Gamma \mathbf{N}_u^\mathsf{T} \, \mathbf{N}_\lambda \, d\Gamma \tag{19}$$

$$\mathbf{L}_b = \int_\Gamma \mathbf{N}_\lambda^\mathsf{T} \, \mathbf{N}_{ub} \, d\Gamma \tag{20}$$

where $\mathbf{A}$ is the global projection matrix, $\mathbf{C}$ the global reciprocal mass matrix, $\mathbf{B}$ the boundary assembly operator and $\mathbf{L}_b$ is the Localized multipliers assembly matrix.

Eliminating symbolically the momentum variable ($\mathbf{p}$) from (13) and (14), one obtains the classical equation of motion expressed in terms of displacements:

$$\left(\mathbf{A}\mathbf{C}^{-1}\mathbf{A}^\mathsf{T}\right)\ddot{\mathbf{u}} + \mathbf{B}\boldsymbol{\lambda} = \mathbf{r} \tag{21}$$

with the mass matrix approximated as:

$$\mathbf{M} = \mathbf{A}\mathbf{C}^{-1}\mathbf{A}^\mathsf{T} \tag{22}$$

and observe that there must exist an inverse mass matrix (denoted as $\mathbf{M}^{-1}$) given by:

$$\mathbf{M}^{-1} = \mathbf{A}^{-\mathsf{T}}\mathbf{C}\mathbf{A}^{-1} \tag{23}$$

assuming that the global projection matrix is invertible.

Since the objective of the present paper is to obtain inverse mass-matrices in efficient and accurate ways, one must insist on easily to invert *diagonal* or narrowly banded projection matrices. This can be accomplished by diagonalizing the projection $\mathbf{A}$-matrix given in (17), leaving the task of constructing the reciprocal $\mathbf{C}$-matrix efficiently and accurately.

2.1. Biorthogonal basis functions

Observing (17) and (23), we realize that a careful selection of the basis functions can simplify the calculation of the mass matrix inverse. For this task, Tkachuk et al. [5] proposed the use of biorthogonal basis functions [15] because they produce a diagonal projection matrix in the form:

$$\mathbf{A}_e = \int_{\Omega_e} \mathbf{N}_u^\mathsf{T}\mathbf{N}_p \, d\Omega, \quad \text{where } [\mathbf{A}_e]_{ij} = 0 \text{ for } i \neq j \tag{24}$$

with a trivial inverse that permits to compute the inverse mass matrix directly from the RMM. We exemplify this in the following simple example.

Example 1

Evaluate the projection matrix and the reciprocal mass matrix for a 1D two-node linear bar element of length L_e and density per unit length ρ_e.

For a two-node linear element with one DOF per node, the basis functions are expressed:

$$\mathbf{N}_u = \begin{bmatrix} \frac{1}{2}(1-\xi) & \frac{1}{2}(1+\xi) \end{bmatrix}$$

and their associated biorthogonal basis functions are given by:

$$\mathbf{N}_p = \begin{bmatrix} \frac{1}{2}(1-3\xi) & \frac{1}{2}(1+3\xi) \end{bmatrix}$$

hence the projection matrix (17) is evaluated as:

$$\mathbf{A}_e = \int_{-1}^{1} \begin{bmatrix} \frac{1}{4}(1-\xi)(1-3\xi) & \frac{1}{4}(1-\xi)(1+3\xi) \\ \frac{1}{4}(1+\xi)(1-3\xi) & \frac{1}{4}(1+\xi)(1+3\xi) \end{bmatrix} \frac{L_e}{2}\, d\xi = \frac{L_e}{2} \begin{bmatrix} 1 & 0 \\ 0 & 1 \end{bmatrix}$$

where we observe that the projection matrix $\mathbf{A}_e$ is diagonal (by design) and indeed equal to the lumped mass matrix computed with unit density. Next, we evaluate analytically the reciprocal mass matrix from its definition (18):

$$\mathbf{C}_e = \int_{-1}^{1} \frac{1}{\rho_e} \begin{bmatrix} \frac{1}{4}(1-3\xi)^2 & \frac{1}{4}(1-3\xi)(1+3\xi) \\ \frac{1}{4}(1+3\xi)(1-3\xi) & \frac{1}{4}(1+3\xi)^2 \end{bmatrix} \frac{L_e}{2}\, d\xi = \frac{L_e}{2\rho_e} \begin{bmatrix} 2 & -1 \\ -1 & 2 \end{bmatrix}$$

and finally use expression (23) to obtain the inverse mass matrix:

$$\mathbf{M}_e^{-1} = \mathbf{A}_e^{-\mathsf{T}} \mathbf{C}_e\, \mathbf{A}_e^{-1} = \frac{2}{\rho_e L_e} \begin{bmatrix} 2 & -1 \\ -1 & 2 \end{bmatrix}$$

to confirm that this is exactly the analytical inverse of the consistent mass matrix. From this simple example, we conclude that it is possible to compute the inverse of the mass matrix without expensive matrix inversions and that, at least for simple linear elements, the result is exact. At the same time, we realize that the projection matrix can be effectively computed from the lumped mass matrix.

However, in presence of Dirichlet boundary conditions or cross-points, things get more complicated because the diagonalization property of the biorthogonal basis functions is lost for the constrained DOFs and the biorthogonal bases need to be modified accordingly [15]. This problem has been extensively studied by Tkachuk et al. [5], that proposed a solution using the following velocity-momentum relation:

$$\mathbf{u} = \begin{Bmatrix} \mathbf{u}_f \\ \bar{\mathbf{u}} \end{Bmatrix} \longrightarrow \begin{bmatrix} \mathbf{I} & \mathbf{A}_d^{\mathsf{T}} \end{bmatrix} \begin{Bmatrix} \dot{\mathbf{u}}_f \\ \bar{\mathbf{v}} \end{Bmatrix} = \mathbf{C}\mathbf{p} \tag{25}$$

where the total displacements $\mathbf{u}$ have been partitioned into free $\mathbf{u}_f$ and fixed $\bar{\mathbf{u}}$. The constrained DOFs produce a populated matrix $\mathbf{A}_d$ that requires special construction, depending upon the element types used and the BC configuration.

Reference [5] discusses various ways of constructing matrices $\mathbf{A}_d$ and $\mathbf{C}$ this way, namely by employing biorthogonal shape functions and inserting penalty terms with adjustable parameters together with somewhat complicated ways of accounting for boundary conditions, etc. This process complicates enormously the formulation. Hence, it is not possible to use, in a straightforward manner, the existing FEM software without considerable modifications. In the present paper, we bypass this procedure and utilize standard FEM data structure.

2.2. An alternative method

For the calculation of the inverse mass matrix, biorthogonal basis functions must be first build for each particular finite element. However, basis functions are known for a limited number of elements, such as line, triangular, quadrilateral and tetrahedral elements. Therefore, we propose a different route for the evaluation of the mass matrix inverse that bypasses this necessity through the following steps:

1. Consider all the structures as free-floating.
2. Approximate the element projection matrix $\mathbf{A}_e$ by a lumping of the element mass matrix.
3. Compute the element reciprocal mass matrix $\mathbf{C}_e$ from a direct inversion of the element mass matrix.
4. Assemble the global projection and reciprocal matrices and compute the global mass matrix inverse.
5. Impose boundary conditions using localized Lagrange multipliers.

The first four steps of this process are described next and the last step, that is a little bit more involved, will be analyzed in the next Section.

First, we consider an element at a time by utilizing the element mass matrices existing in standard FEM software systems. Second, we use the element mass matrix to approximate the element projection matrix by diagonalization, viz.:

$$[\mathbf{A}_e]_{ii} = \frac{1}{\rho_e} \sum_j [\mathbf{M}_e]_{ij} \tag{26}$$

assuming that the density is constant inside the element. Third, the elemental reciprocal mass matrix is evaluated inverting numerically the element mass matrix:

$$\mathbf{C}_e = \mathbf{A}_e^\mathsf{T} \mathbf{M}_e^{-1} \mathbf{A}_e \tag{27}$$

where $(\mathbf{A}_e, \mathbf{C}_e, \mathbf{M}_e)$ are elemental matrices, and particularly $\mathbf{A}_e$ is a diagonalized matrix.

Finally, we proceed with the assembly of the global reciprocal mass matrix:

$$\mathbf{C} = \overset{n_e}{\underset{e=1}{\mathbf{A}}} \mathbf{C}_e \tag{28}$$

and the global projection matrix:

$$\mathbf{A} = \overset{n_e}{\underset{e=1}{\mathbf{A}}} \mathbf{A}_e \tag{29}$$

observing that as long as the elemental $\mathbf{A}_e$ is diagonal, so is the assembled matrix $\mathbf{A}$ and its inverse. These steps permit to evaluate the inverse of the global mass matrix through expression (23) in an efficient way.

3. INCORPORATION OF BOUNDARY CONDITIONS

As we mentioned, in presence of Dirichlet boundary conditions a direct computation of the mass-inverse requires complicated modifications of the biorthogonal shape functions. We eliminate the necessity of these modifications by considering the structures as free-floating and applying the boundary conditions through localized Lagrangian multipliers [11, 12, 13, 14]. To explain the enforcement of boundary conditions, we reorganize the semi-discrete equations of motion (13)-(16) to obtain the following partitioned equation set:

$$\begin{bmatrix} \mathbf{M} & \mathbf{B} & \mathbf{0} \\ \mathbf{B}^\mathsf{T} & \mathbf{0} & -\mathbf{L}_b \\ \mathbf{0} & -\mathbf{L}_b^\mathsf{T} & \mathbf{0} \end{bmatrix} \left\{ \begin{array}{c} \ddot{\mathbf{u}} \\ \boldsymbol{\lambda} \\ \ddot{\mathbf{u}}_b \end{array} \right\} = \left\{ \begin{array}{c} \mathbf{r} \\ \mathbf{0} \\ \mathbf{0} \end{array} \right\} \tag{30}$$

where the second equation is simply twice time-differentiated expression of (15).

Let's assume now that the boundary acceleration vector $(\ddot{\mathbf{u}}_b)$ consists of entirely the prescribed boundary quantities, regardless whether they are zero or nonzero (e.g., ground excitations of earthquakes or car tires rolling on the road). In this case, we obtain the accelerations $(\ddot{\mathbf{u}})$ from the first equation of (30) as:

$$\ddot{\mathbf{u}} = \mathbf{M}^{-1} (\mathbf{r} - \mathbf{B}\boldsymbol{\lambda}) \tag{31}$$

in which once again we emphasize that the computation of $\mathbf{M}^{-1} = \mathbf{A}^{-\mathsf{T}} \mathbf{C} \mathbf{A}^{-1}$ does not requiere additional computational effort because the global projection matrix $\mathbf{A}$ is diagonal.

Then, substitute the accelerations obtained above into the second equation of (30):

$$\mathbf{B}^\mathsf{T} \mathbf{M}^{-1} \left(\mathbf{r} - \mathbf{B} \boldsymbol{\lambda} \right) - \mathbf{L}_b \ddot{\mathbf{u}}_b = \mathbf{0} \tag{32}$$

to compute the Lagrange multipliers:

$$\boldsymbol{\lambda} = \left[\mathbf{B}^\mathsf{T} \mathbf{M}^{-1} \mathbf{B} \right]^{-1} \left(\mathbf{B}^\mathsf{T} \mathbf{M}^{-1} \mathbf{r} - \mathbf{L}_b \ddot{\mathbf{u}}_b \right) \tag{33}$$

and substitute them back in (31) to obtain the final accelerations:

$$\ddot{\mathbf{u}} = \mathbf{M}_b^{-1} \mathbf{r} + \mathbf{M}^{-1} \mathbf{B} \left[\mathbf{B}^T \mathbf{M}^{-1} \mathbf{B} \right]^{-1} \mathbf{L}_b \ddot{\mathbf{u}}_b \tag{34}$$

with a constrained inverse mass matrix:

$$\mathbf{M}_b^{-1} = \mathbf{M}^{-1} - \mathbf{M}^{-1} \mathbf{B} \left[\mathbf{B}^\mathsf{T} \mathbf{M}^{-1} \mathbf{B} \right]^{-1} \mathbf{B}^\mathsf{T} \mathbf{M}^{-1} \tag{35}$$

defined as the inverse mass matrix incorporating the applied boundary conditions. Once again, since the size of $\left[\mathbf{B}^T \mathbf{M}^{-1} \mathbf{B} \right]$ is small, pertaining to the boundary degrees of freedom, its inversion is trivial. Notice that when the structure is free-free, one has $\mathbf{B} = \mathbf{0}$ so that $\mathbf{M}_b^{-1}$ is simply the inverse mass matrix.

It is also noted that the degrees of freedom for $\ddot{\mathbf{u}}$ consists of not only the interior ones but also the constrained boundary displacements. Consequently, $\mathbf{M}_b^{-1}$ would be singular corresponding to the constrained boundary degrees of freedom. One way to eliminate the almost singular mass matrix is simply to eliminate the rows and columns of $\mathbf{M}_b^{-1}$ corresponding to the boundary degrees of freedom. Its justification will be examined next.

3.1. Projection of the mass matrix

The proposed element-independent and biorthogonal-free derivation of the global inverse mass matrix described in Section 2.2 and subsequent evaluation of final accelerations through (34), can be elegantly expressed as:

$$\ddot{\mathbf{u}} = \mathbf{M}_b^{-1} \mathbf{r} + (\mathbf{I} - \boldsymbol{\mathcal{P}}) \mathbf{L}_b \ddot{\mathbf{u}}_b \tag{36}$$

where we understand the constrained inverse (35) as a projection of the free-floating inverse mass matrix on a subspace incorporating the boundary constrains, i.e.:

$$\mathbf{M}_b^{-1} = \boldsymbol{\mathcal{P}} \mathbf{M}^{-1} \tag{37}$$

with an operator:

$$\boldsymbol{\mathcal{P}} = \mathbf{I} - \mathbf{M}^{-1} \mathbf{B} \left[\mathbf{B}^\mathsf{T} \mathbf{M}^{-1} \mathbf{B} \right]^{-1} \mathbf{B}^\mathsf{T} \tag{38}$$

that projects any acceleration vector on the subspace of accelerations, automatically fulfilling the zero boundary conditions ($\ddot{\mathbf{u}}_b = \mathbf{0}$).

Projector (38) presents the following two interesting properties:

$$\mathbf{B}^\mathsf{T} \boldsymbol{\mathcal{P}} = \mathbf{0} \tag{P1}$$

$$\boldsymbol{\mathcal{P}} \mathbf{M}^{-1} \mathbf{B} = \mathbf{0} \tag{P2}$$

that will be used next to derive some important conclusions.

Proposition 2
The rows and columns of $\mathbf{M}_b^{-1}$ corresponding to constrained DOFs are identically zero.

Proof
Note that pre and post multiplication by the boundary extraction operator $\mathbf{B}$ selects the rows and columns corresponding to constrained DOF positions. Thanks to properties (P1) and (P2) we find that,

$$\mathbf{B}^\mathsf{T} \boldsymbol{\mathcal{P}} \mathbf{M}^{-1} \mathbf{B} = \mathbf{0}$$

$\square$

Step I: Assemble diagonal projection matrix:

$$[\mathbf{A}_e]_{ii} = \frac{1}{\rho_e} \sum_j [\mathbf{M}_e]_{ij} \quad \longrightarrow \quad \mathbf{A} = \overset{n_e}{\underset{e=1}{\mathbf{A}}} \mathbf{A}_e$$

Step II: Assemble reciprocal mass matrix:

$$\mathbf{C}_e = \mathbf{A}_e^\mathsf{T} \mathbf{M}_e^{-1} \mathbf{A}_e \quad \longrightarrow \quad \mathbf{C} = \overset{n_e}{\underset{e=1}{\mathbf{A}}} \mathbf{C}_e$$

Step III: Evaluate free-floating inverse mass matrix:

$$\mathbf{M}^{-1} = \mathbf{A}^{-\mathsf{T}} \mathbf{C} \mathbf{A}^{-1}$$

Step IV: Compute projector:

$$\boldsymbol{\mathcal{P}} = \mathbf{I} - \mathbf{M}^{-1}\mathbf{B} \left[\mathbf{B}^\mathsf{T}\mathbf{M}^{-1}\mathbf{B} \right]^{-1} \mathbf{B}^\mathsf{T}$$

Step V: Apply boundary conditions by projection:

$$\mathbf{M}_b^{-1} = \boldsymbol{\mathcal{P}}\mathbf{M}^{-1}$$

Step VI: Eliminate rows and columns of $\mathbf{M}_b^{-1}$.

Table I. Procedure for the computation of the constrained inverse mass matrix $\mathbf{M}_b^{-1}$.

Proposition 3
Projector $\boldsymbol{\mathcal{P}}$ applied to the free-floating body accelerations of the system $\mathbf{a}_{free} = \mathbf{M}^{-1}\mathbf{r}$, imposes zero Dirichlet boundary conditions to the constrained DOFs.

Proof
Note from (36) that, if the boundary conditions are zero ($\ddot{\mathbf{u}}_b = \mathbf{0}$), the final accelerations can be written as:

$$\ddot{\mathbf{u}} = \boldsymbol{\mathcal{P}}\mathbf{a}_{free}$$

and thanks to property (P2) we also observe that the projector filters out the unbalanced-force components ($\mathbf{Br}$) associated to the fixed DOFs, i.e.:

$$\ddot{\mathbf{u}} = \boldsymbol{\mathcal{P}}\mathbf{M}^{-1}\left[\mathbf{Br} + (\mathbf{I} - \mathbf{B})\mathbf{r}\right] = \boldsymbol{\mathcal{P}}\mathbf{M}^{-1}\left(\mathbf{I} - \mathbf{B}\right)\mathbf{r}$$

where $(\mathbf{I} - \mathbf{B})\mathbf{r}$ are the external-internal residual forces of the free DOFs.   □

As a summary, the complete process followed to obtain the inverse mass matrix $\mathbf{M}^{-1}$ and the projector $\boldsymbol{\mathcal{P}}$ is contained in Table I. Note that in dynamic analyses the product of these two matrices $\mathbf{M}_b^{-1}$ is never evaluated explicitly. Hence the two-step solution process consists of multiplying the residual by the mass-inverse to compute free-floating body accelerations and later by the projector to apply boundary conditions. Multiplication of the projector times a vector requires also the factorization of $\mathbf{B}^\mathsf{T}\mathbf{M}^{-1}\mathbf{B}$, but this is a small matrix of size equal to the number of BCs.

4. SELECTIVE MASS SCALING

In classical explicit time-integration methods, maximum time-step size for stability is controlled by the highest natural frequency of the system [16]. The basic idea behind selective mass scaling [17, 18, 19, 20, 21] is to alter the mass matrix artificially in order to reduce the high frequencies of the dynamical system without affecting the low-mid frequencies.

In this Section, we propose a simple method to reduce the highest frequencies of the system that can be combined with the proposed mass matrix inverse method for best efficiency. The mass scaling process is applied element by element. To start, the original mode shapes of the element are

first computed by solving the eigenvalue problem:

$$\mathbf{K}_e\mathbf{X}_e = \mathbf{M}_e\mathbf{X}_e\mathbf{\Lambda}_e \tag{39}$$

where $\mathbf{X}_e$ is the matrix containing the orthogonal mode shapes of the element and the diagonal matrix $\mathbf{\Lambda}_e = \mathbf{X}_e^{\mathsf{T}}\mathbf{K}_e\mathbf{X}_e$ contains the original eigenfrequencies of the problem.

The n orthogonal mode shapes of the element can be separated into high and low frequency modes in the form:

$$\mathbf{X}_e = [\mathbf{\Phi}_l,\ \mathbf{\Phi}_h] \tag{40}$$

where we have r retained low-frequency modes $\mathbf{\Phi}_l$ and $s = n - r$ scaled high frequency modes $\mathbf{\Phi}_h$.

In order to scale only the high frequency modes of the element, without affecting the low frequency modes at the same time, we define a new projector:

$$\mathcal{P}_e = \mathbf{I} - \mathbf{\Phi}_l\left[\mathbf{\Phi}_l^{\mathsf{T}}\mathbf{\Phi}_l\right]^{-1}\mathbf{\Phi}_l^{\mathsf{T}} \tag{41}$$

with the following filtering property:

$$\mathcal{P}_e\mathbf{X}_e = [\mathbf{0},\ \mathbf{\Phi}_h] \tag{P3}$$

and then modify the element mass matrix in the form:

$$\mathbf{M}_e^{\alpha} = \mathbf{M}_e + \alpha\mathcal{P}_e^{\mathsf{T}}\mathbf{M}_e\mathcal{P}_e \tag{42}$$

where $\alpha \geq 0$ is a mass scaling parameter.

Proposition 4
With the mass scaled matrix $\mathbf{M}_e^{\alpha}$, the high frequencies of the element are scaled by a factor $(1 + \alpha)^{-1}$ maintaining the element low frequencies unaffected, i.e., the new element eigenvalues are given by the diagonal matrix:

$$\mathbf{\Lambda}_e^{\alpha} = \begin{bmatrix} \mathbf{I}_r & \mathbf{0} \\ \mathbf{0} & (1+\alpha)^{-1}\mathbf{I}_s \end{bmatrix}\mathbf{\Lambda}_e$$

with the same modes $\mathbf{X}_e$ than the original element.

Proof
It is very simple to demonstrate that the new scaled-mass eigenvalue problem:

$$\mathbf{K}_e\mathbf{X}_e = \left(\mathbf{M}_e + \alpha\mathcal{P}_e^{\mathsf{T}}\mathbf{M}_e\mathcal{P}_e\right)\mathbf{X}_e\mathbf{\Lambda}_e^{\alpha}$$

has exactly the same eigenvectors than the original one, with the same r low frequencies and s reduced high frequencies. This is demonstrated premultiplying by $\mathbf{X}_e^{\mathsf{T}}$ that produces, thanks to property (P3), the new eigenvalues:

$$\mathbf{\Lambda}_e = \left(\mathbf{I}_n + \alpha\left[\mathbf{0},\ \mathbf{\Phi}_h\right]^{\mathsf{T}}\mathbf{M}_e\left[\mathbf{0},\ \mathbf{\Phi}_h\right]\right)\mathbf{\Lambda}_e^{\alpha} = \left(\mathbf{I}_n + \begin{bmatrix} \mathbf{0}_r & \mathbf{0} \\ \mathbf{0} & \alpha\mathbf{I}_s \end{bmatrix}\right)\mathbf{\Lambda}_e^{\alpha}$$

from where we can obtain $\mathbf{\Lambda}_e^{\alpha}$ inverting a simple diagonal matrix. □

It remains the selection of appropriated values for the scaling parameter α and the number of modes to scale s that will be analyzed in the next Section.

It is important to mention that, although different mass-scaling methods have been proposed by other authors [22, 23, 24], the proposed mass-scaling technique is defined as selective in the sense that we can choose the number of modes to scale and this scaling is performed at the element level.

5. NUMERICAL EXPERIMENTS

Although the proposed techniques for mass matrix inversion and scaling can be equally applied to linear and non-linear constitutive models, we will assume linear-elastic materials in our numerical experiments with internal forces simply given by the linear relation $\mathbf{f}^{int} = \mathbf{K}\mathbf{u}$. We have assessed the performance of the present mass matrix inverse for bar, beam, solid and shell structural elements, in both free-free states and cantilevered conditions. In so doing, for the derivation of elemental reciprocal mass matrix $\mathbf{C}_e$, we have utilized a parametrized elemental mass matrix expressed in the form:

$$\mathbf{M}_e = (1 - \beta)\mathbf{M}_e^c + \beta\mathbf{M}_e^l \tag{43}$$

in which a parameter $\beta \in [0, 1]$ is used to balance between the consistent element mass matrix $\mathbf{M}_e^c$ and the lumped element mass matrix $\mathbf{M}_e^l$. Using $\beta = \{0, 0.5, 1\}$ the element mass matrix is then easily reduced respectively to the consistent mass matrix (CMM), averaged mass matrix (AMM) and lumped mass matrix (LMM). Unless otherwise stated, in the following numerical experiments we employ AMM as a reference and compute the mass matrix inverse using RMM with $\beta = 0.5$ to test the proposed methodology. There are several ways to parametrize mass matrices, for example see Felippa et al. [4] for an exhaustive classification. Among them, spectral parametrization (42) and matrix-weighted linear parametrization (43) are the simplest choices.

For vibration analyses we seek for an harmonic solutions that satisfy the EOM and fulfill the boundary conditions $\mathbf{u}_b = \mathbf{0}$. These solutions are obtained by solving the following eigenvalue problem:

$$\left[\mathbf{M}_b^{-1}\mathbf{K}_b - \omega^2\mathbf{I}\right]\phi = \mathbf{0} \tag{44}$$

where $\mathbf{M}_b^{-1}$ is the inverse mass matrix computed as described in Section 3 and $\mathbf{K}_b$ is the stiffness matrix incorporating the applied boundary conditions. From the solution of this eigenvalue problem, we obtain the vibration frequencies ω_i of the system and its associated mode shapes ϕ_i for mode number $i = 1, \ldots n$.

In time-domain analyses, for time integration of the semi-discrete equations of elastodynamics, we use the classical explicit central difference scheme [25, 26, 27]. This method is among the most popular explicit methods in computational mechanics [28] and can be summarized in the following steps:

1. Knowing from previous time $\mathbf{u}^n$ and $\dot{\mathbf{u}}^{n-\frac{1}{2}}$

2. Evaluate the forces residual $\mathbf{r}^n = \mathbf{f}^n - \mathbf{K}_b\mathbf{u}^n$

3. Compute accelerations $\ddot{\mathbf{u}}^n = \mathbf{M}_b^{-1}\mathbf{r}^n$

4. Update nodal velocities $\dot{\mathbf{u}}^{n+\frac{1}{2}} = \dot{\mathbf{u}}^{n-\frac{1}{2}} + \Delta t\ddot{\mathbf{u}}^n$

5. Update nodal displacements $\mathbf{u}^{n+1} = \mathbf{u}^n + \Delta t\dot{\mathbf{u}}^{n+\frac{1}{2}}$

6. Advance time $n \leftarrow n + 1$

repeating these basic steps until the total simulation-time has been reached.

It is well known that the explicit central difference scheme in linear dynamics is conditionally stable, so the time-step Δt must be chosen below a critical value $\Delta t_{crit} = 2/\omega_{max}$, where ω_{max} is the maximum frequency of the system. Selective mass scaling techniques, like the one proposed in Section 4, permits a localized reduction of the highest eigenvalues of the system by a certain factor. This reduction automatically increases the critical time-step, improving computational efficiency.

5.1. Frequencies of a free-free and a fixed-free bar

In this first example, we consider a long bar of length $L = 1m$ with a rectangular section of width $b = 0.05$ m and thickness $h = 0.01$ m. The material of the bar is linear elastic, with Young's modulus $E = 69$ GPa and a constant density $\rho = 2700 \, \text{kg/m}^3$. We discretize the bar using a uniform mesh of 40 two-node linear bar elements and compute the vibration modes of the structure with different
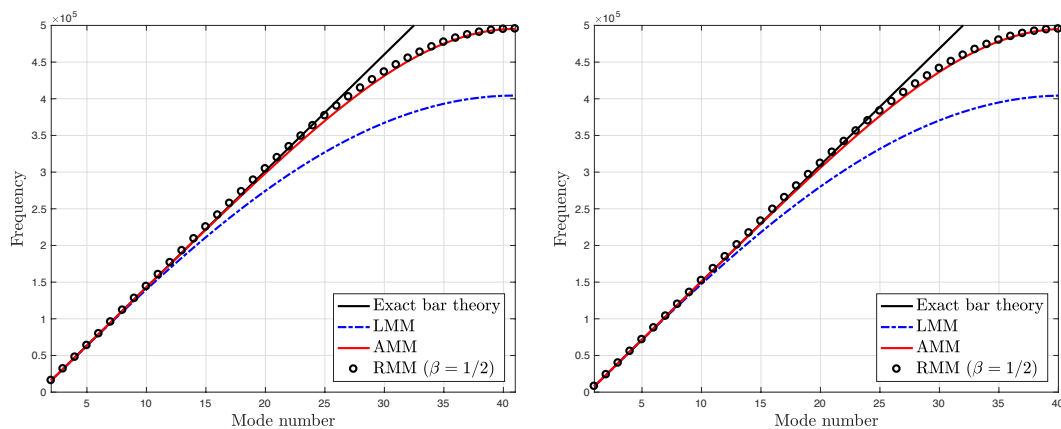
Figure 1. Bar vibration problem. Frequencies for the free-free (left) and fixed-free (right) cases. Comparison of exact frequencies and numerical frequencies obtained with: lumped mass matrix (LMM), average mass matrix (AMM) and the proposed inverse mass matrix (RMM $\beta = 0.5$).

approximations for the mass matrix inverse. In particular, we investigate differences in the use of the lumped mass matrix LMM, averaged mass matrix AMM and the proposed mass matrix inverse computed through RMM with $\beta = 0.5$.

The results of the eigenvalue analysis are presented in Figure 1 for two different boundary conditions, free-free case (left) and fixed-free case (right). We start with the free-free case, by comparing the numerical frequencies with the exact solution obtained from continuum theory. The exact frequencies of this problem are $\omega_i^{exact} = \sqrt{E/\rho}(\pi/L)(i-1)$ rad/sec for mode number $i = 1, \ldots n$ and the first eigenfrequency is zero, corresponding to the horizontal rigid body motion. We observe that the present method, utilizing the RMM, yields far better accuracy than the LMM and approximates very well to the AMM results for all frequencies.

For the fixed-free case, we obtain very similar results. The only difference now is in the restriction of the rigid body motion and the shift of exact frequencies to $\omega_i^{exact} = \sqrt{E/\rho}(\pi/L)(i-1/2)$ rad/sec for mode number $i = 1, \ldots n$. We corroborate that the AMM and its approximation through the RMM with $\beta = 0.5$ provides exactly the same result. This means that the present method utilizing the inverse mass matrix yields far better accuracy than the lumped mass matrix with similar computational effort.

It can also be observed that LMM produces a maximum frequency around 20% lower than AMM, so the critical time-step for explicit time-integration can be reduced by the same amount using a diagonal mass matrix. As we will see later, even higher gains can be obtained with the selective mass scaling technique proposed in Section 4, maintaining at the same time the advantages in terms of accuracy of using a non-diagonal mass matrix.

5.1.1. Free-free heterogeneous bar. The effect of material heterogeneity in the accuracy of the direct mass inverse is next investigated by dividing the free-free bar into two segments of different density, see Figure 2 (left) for a description of the new configuration. The exact angular frequencies for this new case are $\omega_i^{exact} = (\pi/L_1)(i-1)(c_1 c_2)/(c_1 + c_2)$ where $c_j = \sqrt{E_j/\rho_j}$ with $j = 1, 2$ is the velocity of compressional waves in material j.

A relatively coarse regular mesh of 5 elements is selected to discretize each part of the bar and the frequencies are recalculated first using AMM and RMM ($\beta = 0.5$) without partitioning the domain. The results are represented in Figure 2 (right) together with the numerical values contained in Table II. In general the accuracy of the six first non-zero modes is very good, but a congruent application of the proposed methodology to this case requires a partitioning the domain into different homogenous subdomains interconnected using localized Lagrange multipliers. In this case, a computation of frequencies with RMM ($\beta = 0.5$) partitioning the problem into two different subdomains produces exactly the same global frequencies, contained in the third row of Table II.
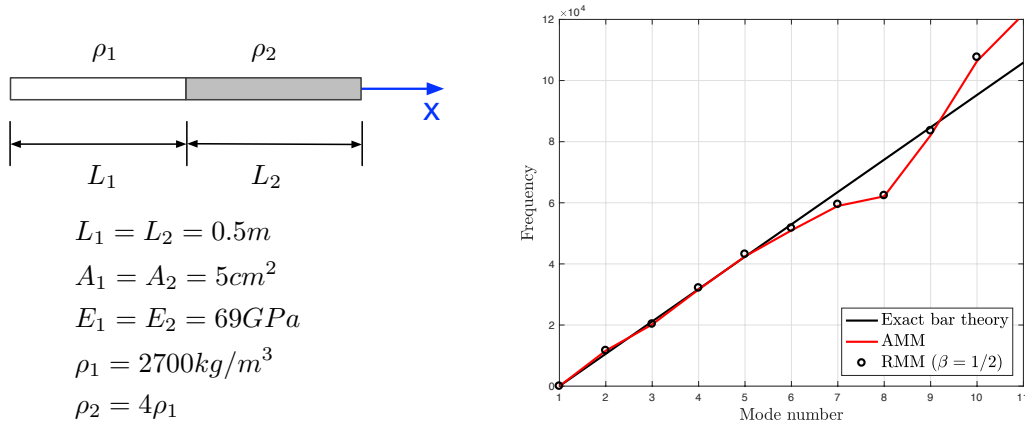
Figure 2. Heterogenous bar problem. Setup of the free-free bi-material bar (left). Comparison of the exact angular frequencies with numerical frequencies computed using the average mass matrix (AMM) and the proposed inverse mass matrix (RMM $\beta = 0.5$) without partitioning the domain (right).

Frequency (Hz) $\times 10^{-4}$	Mode 2	Mode 3	Mode 4	Mode 5	Mode 6	Mode 7
AMM	0.1848	0.3213	0.5033	0.6757	0.8112	0.9383
RMM no partitioning	0.1853	0.3235	0.5116	0.6871	0.8234	0.9468
RMM partitioning	0.1853	0.3233	0.5114	0.6851	0.8224	0.9468

Table II. Free-free two material rod. Frequencies of the first six non-zero modes obtained with the AMM and the proposed RMM using one domain and partitioning the bar into two subdomains.
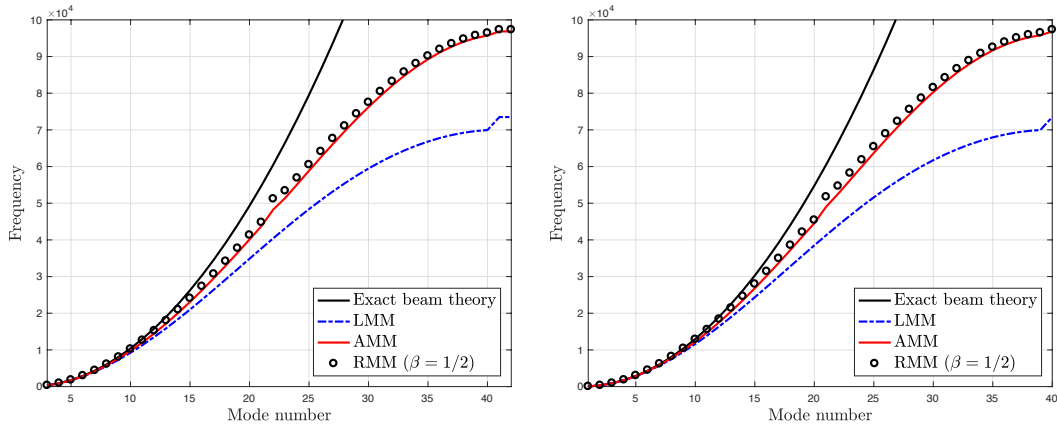
Figure 3. Beam vibration problem. Frequencies for the free-free (left) and fixed-free (right) cases. Comparison of exact frequencies and numerical frequencies obtained with: lumped mass matrix (LMM), average mass matrix (AMM) and the proposed inverse mass matrix (RMM $\beta = 0.5$).

5.2. Frequencies of a free-free and a fixed-free beam

In this second case, we consider the same geometry of the previous example but now it is discretized using 20 Euler-Bernoulli beam elements with two DOFs per node, i.e., deflection and rotation. We know that the shape functions for the Euler-Bernoulli beam require C^1-continuity for deflections and rotations, hence cubic Hermite polynomials are used as interpolation functions. This means that we would need to derive biorthogonal basis functions for the Hermite cubic shape functions in order to compute the reciprocal mass matrix $\mathbf{C}_e$ from its definition (18). As previously described, we bypass this complex derivation obtaining the projection matrix $\mathbf{A}_e$ from the diagonalization of the element mass matrix.
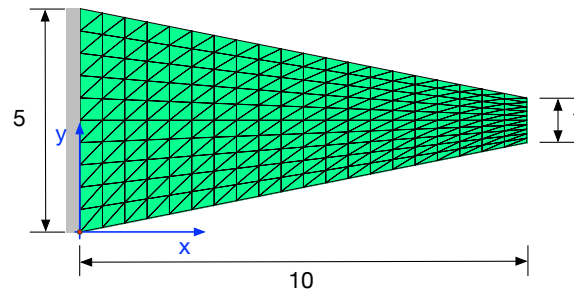
Figure 4. NAFEMS benchmark case FV32. Geometry, mesh and dimensions in meters. The thickness of the plate is $t = 0.05$ m and zero boundary displacements are imposed on the lateral side.

In Figure 3 (left) we analyze the frequencies obtained for the free-free beam case. The exact frequencies of this problem obtained from continuum theory are $\omega_i^{exact} = \sqrt{EI/\rho A}(c_i/L)^2$ rad/sec with $c = \{0, 0, 4.73, 7.853, 10.996, 14.137, 17.279, \dots\}$ for mode number $i = 1, \dots n$ and two zero frequencies corresponding to the displacement and rotation rigid-body motions. We solve again the problem with exact LMM and AMM inverse mass-matrices and then using the proposed RMM with $\beta = 0.5$. Results illustrate, first, that the consistent AMM gives far better accuracy than diagonal LMM for this particular case, specially in the high-frequency range. Secondly, that the present RMM method utilizing the inverse mass matrix yields the same accuracy than the consistent AMM.

The results for the fixed-free alternative of this problem are represented in Figure 3 (right). The exact frequencies of this case are $\omega_i^{exact} = \sqrt{EI/\rho A}(c_i/L)^2$ rad/sec with $c = \{1.875, 4.694, 7.854, 10.995, 14.131, 17.278, \dots\}$. Exactly the same precision is observed in the free-free and fixed-free solutions. This convinces us to the conclusion that the described method for generating the inverse of mass matrices $\mathbf{M}_b^{-1}$, yields almost the same resonant frequencies as those obtained by the consistent mass matrices, as evidenced from Figure 3, thus confirming the validity of the present formulation.

5.3. Frequency analysis of a cantilevered tapered plate

Our third example is a plane-stress test proposed by the National Agency for Finite Element Methods and Standards [29]. In particular the dynamic case FV32, where the natural frequencies of a trapezoidal elastic plate are analyzed. The geometry and dimensions of the plate are represented in Figure 4 together with the boundary conditions. A linear elastic material with Young's modulus $E = 200$ GPa, Poisson's ratio $\nu = 0.3$, and density $\rho = 8000 \, \text{kg/m}^3$ is assumed. The plate is discretized using a regular mesh composed of 231 nodes and 400 triangular linear finite elements, constraining the horizontal and vertical displacements of the 11 nodes located at $x = 0$, a lateral side of the plate. Note that this is a more refined mesh than the one proposed in the original NAFEMS benchmark case, that uses quadrilateral elements instead of triangles and doubles the element size.

We perform a frequency analysis solving the eigenvalue problem (44) using different mass-matrices. In particular, we consider the consistent mass matrix CMM and the average mass matrix AMM, that are compared with their equivalent RMMs obtained with $\beta = 0$ and $\beta = 0.5$.

The first six mode shapes of the plate are illustrated in Figure 5 and their associated frequencies, obtained with the different mass-matrices, arranged in Table III. Notice that, in the original NAFEMS results, mode shapes 5 and 6 are interchanged. In our case, mode 5 appears at a little higher frequency because it is a pure longitudinal symmetric mode and our mesh made of triangles is not symmetric.

Tkachuk et al. [5] solved this problem using the same mesh and the RMM. When comparing with their results, the maximum difference is obtained in the sixth frequency with an error below 2% while the best fit is obtained for RMM with $\beta = 0.5$. On the other hand, comparing the frequencies obtained using our exact implementation of the CMM with the reciprocal mass-inverse RMM technique, errors reduce to the second decimal digit. It is also observed that averaging the
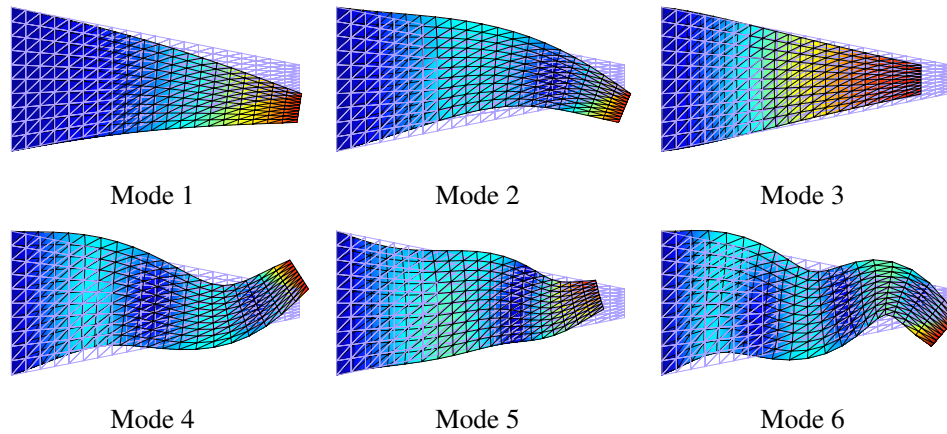
Figure 5. NAFEMS benchmark case FV32. Representation of the six lowest vibration modes occurring at frequencies contained in Table III. Results correspond to RMM with $\beta = 0.5$.

Frequency (Hz)	Mode 1	Mode 2	Mode 3	Mode 4	Mode 5	Mode 6
NAFEMS	44.623	130.03	162.70	246.05	379.90	391.44
Tkachuk et al. [5]	45.499	133.55	162.89	255.37	393.16	398.56
CMM	45.42	132.60	162.73	251.40	387.40	391.16
RMM ($\beta = 0$)	45.42	132.60	162.73	251.40	387.40	391.18
AMM	45.46	133.08	162.81	253.36	391.72	393.32
RMM ($\beta = 0.5$)	45.48	133.33	162.85	254.37	392.56	395.68

Table III. Plane-stress case from NAFEMS. Six lowest frequencies obtained with different mass matrices. Legends - AMM: averaged mass matrix, CMM: consistent mass matrix, RMM: proposed reciprocal mass matrix.

mass matrix increases slightly the error to a 0.6% in the sixth mode. In general, it is verified that the proposed mass-inversion process gives very accurate approximations of the CMM and AMM inverses.

5.4. Transient analysis of a cantilever beam under tip load

To test the solid tetrahedral element, we use the cantilever beam with vertical load proposed Olovsson et al. in [19] also studied by Tkachuk et al. [5] to investigate the accuracy of direct mass-inverse methods. The geometrical definition of the problem is shown in Figure 6, where a cantilever beam of length $L = 0.1$ m and section height $b = 0.003$ m with thickness $t = 0.001$ m is considered. Material properties of the beam are $E = 207$ GPa, $\nu = 0.3$ and $\rho = 7800 \, \mathrm{kg/m^3}$.

The beam is discretized using a regular mesh of 408 nodes and 900 tetrahedral elements, with $50 \times 3 \times 1$ divisions per side. One end of the beam is completely fixed and the other side has two vertical point loads of value $f = -1$ N.

In this case, we perform a time-domain analysis integrating in time the response of the beam using the explicit central difference method. Initial conditions of the beam are assumed to be zero displacements and velocities, applying the tip load completely at the initial time-step. We have selected for comparison the exact AMM and the proposed inverse through RMM computed with $\beta = 0.5$.

The results are shown in Figure 7, where it is represented the evolution of the tip deflection of the beam obtained with both mass-matrices (left). We also compare the time evolution of total internal U, external W and kinetic T energies of the beam (right).

In Figure 8 (left) is represented the relative error $(u - u_{exact})/|u_{exact}|$ of the tip displacement, computing u with the RMM inverse mass matrix and u_{exact} with the exact AMM. The error remains
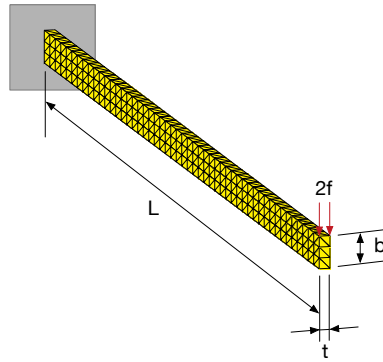
Figure 6. Cantilever beam with tip load. Geometry, mesh and dimensions.
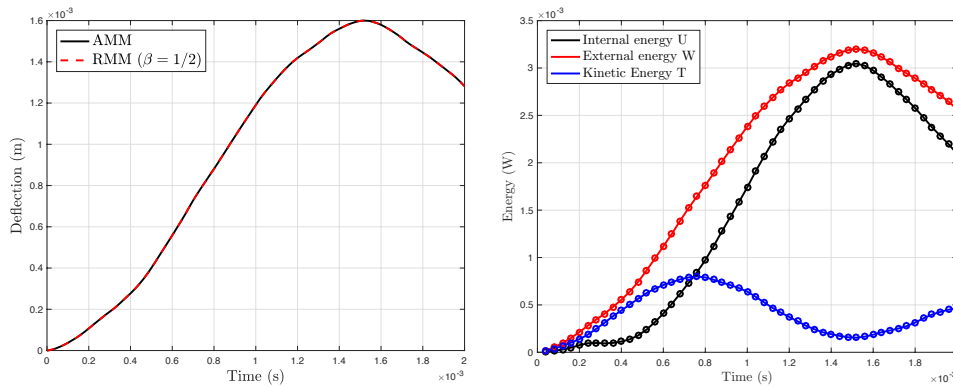

Figure 7. Results of the tip loaded cantilever beam. Tip deflection $|u_z|$ computed with the exact averaged mass matrix AMM and the reciprocal mass matrix RMM ($\beta = 0.5$) (left). Evolution of the internal, external and kinetic energies in the beam (right). Solutions obtained using the proposed RMM inverse matrix are represented with dots.
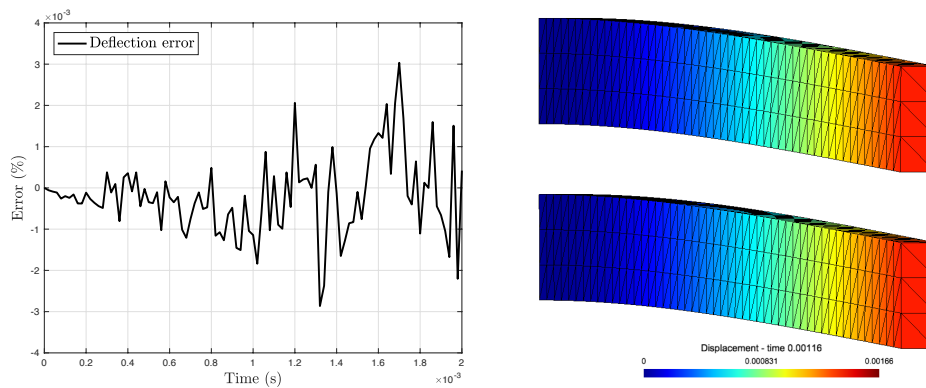

Figure 8. Error of the cantilever beam solution. Error evolution of the beam tip deflection computed with RMM ($\beta = 0.5$) compared to AMM. Displacement contours at $t = 0.0016s$ (right), computed with the exact average mass matrix AMM (bottom) and the proposed reciprocal mass matrix RMM ($\beta = 0.5$) (top).

under 0.003% during the 0.002 s of simulation, indicating a perfect agreement. Displacement contours obtained with both methods at time $t = 1.16$ ms are represented in Figure 8 (right). Differences between RMM displacements (top) and AMM displacements (bottom) can not be perceived. It is also noted that, although the problem is perfectly symmetric, a small lateral displacement appears in the solution due to the asymmetry introduced by the mesh.
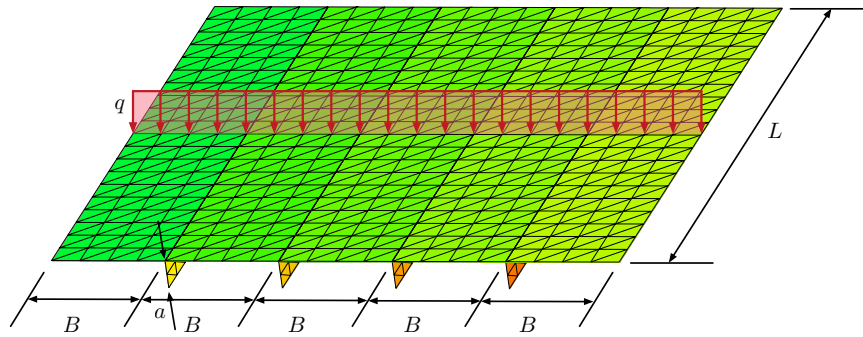
Figure 9. Geometrical definition of a simply supported plate with four stiffeners and loaded by a constant line load at the center of the plate.
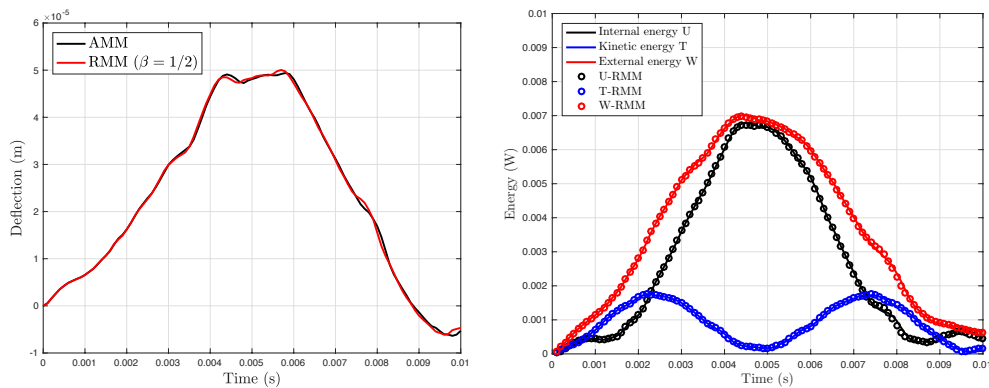

Figure 10. Results of the stiffened plate problem. Deflection at the center of the plate (left) and evolution of the total kinetic, internal and external energies (left) computed with the average mass matrix (AMM) and the reduced mass matrix (RMM) inverse.

5.5. Transient analysis of a panel

In this example we analyze the inverse mass matrix of a structural 3-node shell element with six DOFs per node. The consistent mass matrix of the 18 DOF shell element is computed by separating membrane and bending contributions, where the membrane component is obtained from the plane triangular linear element while the normal and bending mass from three equivalent fictitious beams located on the element edges. Therefore, we are applying the proposed mass-inverse methodology to a complicated structural mass matrix that would be difficult to invert by other means.

The selected test problem is represented in Figure 9, a simply supported panel constructed using a square plate of side length $L = 1$ m and four longitudinal stiffeners separated a constant distance $B = 0.2$ m. The stiffeners, attached on one side the plate, have a section height $a = 0.05$ m and all components have the same thickness $t = 0.01$ m. For the material properties, we consider a steel with Young's modulus $E = 207$ GPa, Poisson coefficient $\nu = 0.3$ and density $\rho = 7850 \, \text{kg/m}^3$.

The plate is modeled using a regular mesh of $20 \times 20 \times 2$ elements and each stiffener has $20 \times 2 \times 2$ elements, with a total number of 1120 shell elements and 609 nodes. All the boundary nodes of the plate have restricted displacements in the three directions and the panel is loaded by a transversal constant line load of value $q = 200$ N/m that is abruptly applied at time zero.

An explicit time integration of the problem is performed for 10 ms using the central difference method. The results are shown in Figure 10 (left) where it is compared the deflection in the center of the plate obtained with the average mass matrix (AMM) and the reduced mass matrix (RMM) inverse with $\beta = 0.5$. Figure 10 (right) represents the evolution of the total kinetic, internal and external energies computed with both methods.
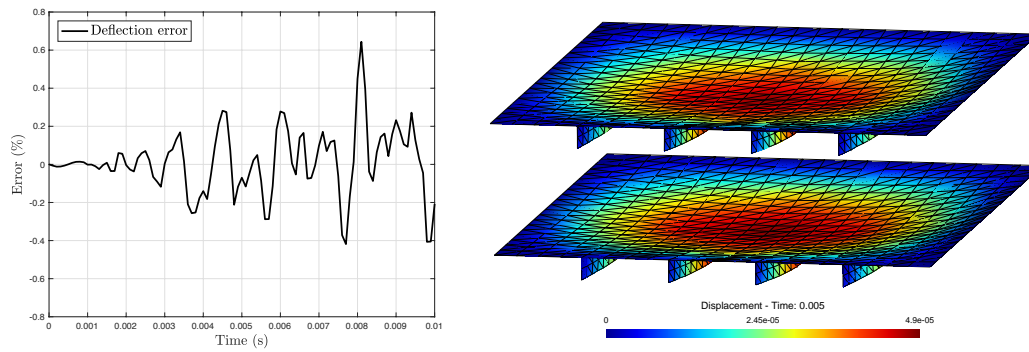
Figure 11. Error in the deflection obtained with exact mass matrix and using proposed inverse mass (right). Displacement contours at $t = 5$ ms (right) obtained with exact AMM (bottom) and using proposed inverse through the CMM (top).
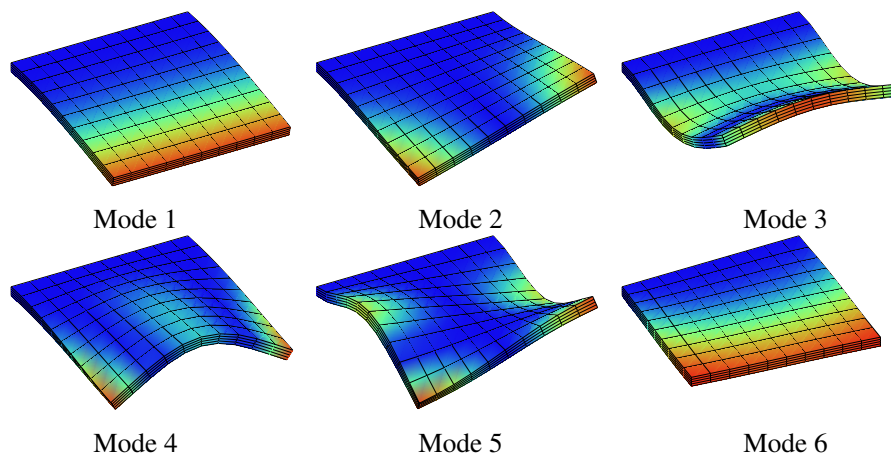

Figure 12. First six mode shapes of the 3D cantilever plate model. Representation of the six lowest vibration modes occurring at frequencies contained in Table IV. Results correspond to RMM with 18 scaled modes and a scaling parameter $\alpha = 100$.

In this case, although some small differences are observed in the solutions, the error is perfectly acceptable for engineering purposes. The deflection errors obtained in the center of the plate, see Figure 11 (left), remain under 0.6% during the simulation period and the structural deformations obtained with AMM and RMM inverses are completely indistinguishable, as demonstrated by the contour solutions at time $t = 5$ ms compared side by side in Figure 11 (right).

5.6. Mass scaling of a cantilever plate

The purpose of this last example is to test the selective mass scaling technique proposed in Section 4. For that, we consider a square cantilever plate of side length $L = 10$ m and thickness $t = 0.5$ m, made of a structural steel with Young's modulus $E = 207$ GPa, Poisson's coefficient $\nu = 0.3$ and $\rho = 7800 \, \text{kg/m}^3$.

The plate is discretized with three-dimensional 8-node solid elements, using a structured mesh of 10 elements per side and 4 elements across the thickness, with a total of 400 brick elements and 605 nodes. Zero displacement boundary conditions are imposed in the three directions to all the nodes lying on one side of the plate and the eigenvalue problem (44) is solved for all the frequencies with a scaled mass matrix. The vibration mode shapes of the plate are represented in Figure 12 for the six lowest frequencies and their associated frequencies are contained in the first row of Table IV.

With the intention of reducing the highest frequencies of the resulting FEM equations, corresponding to the so-called mesh frequencies, without affecting the lower physical frequencies,

Frequency (Hz)	Mode 1	Mode 2	Mode 3	Mode 4	Mode 5	Mode 6
No scaling	6.7703	12.0809	42.0886	47.7580	50.3711	54.6703
Scaling ($\alpha = 1$)	6.8151	12.3473	43.7787	50.6586	53.0128	54.9494
Scaling ($\alpha = 10$)	6.8147	12.3399	43.7571	50.5726	52.8431	54.8953
Scaling ($\alpha = 100$)	6.8141	12.3356	43.7325	50.5274	52.7784	54.8702

Table IV. Cantilever plate model. Effect of mass scaling on the first six natural frequencies of the system. These results correspond to the case $s = 12$ scaled modes, represented in Figure 13 (right).
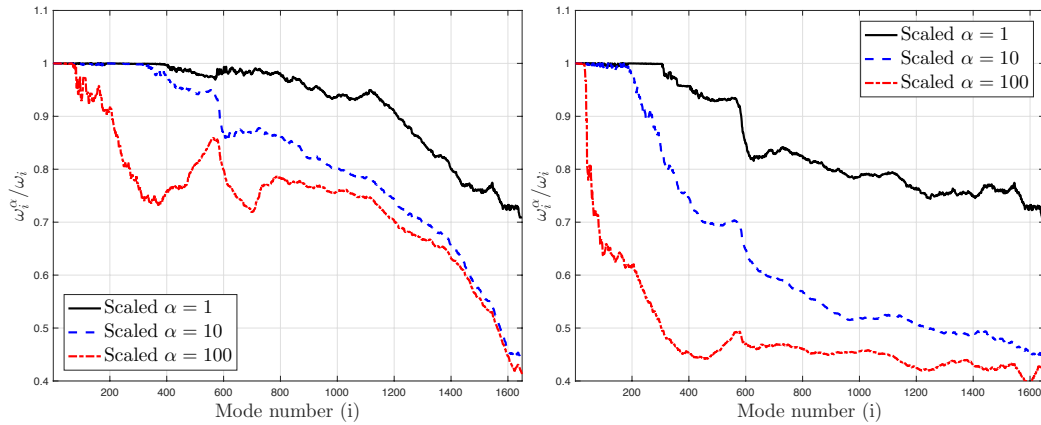
Figure 13. Relation of scaled/exact frequencies for the cantilever plate model. Effect of the scaling parameter α and the number of scaled modes s on the complete range of system frequencies. Number of scaled element modes are $s = 6$ (left) and $s = 12$ (right) and the highest element modes are scaled by a factor $(1 + \alpha)^{-1}$.

we proceed with a scaling of the mass matrix increasing the values of the scaling parameter to $\alpha = \{1, 10, 100\}$. This is made for two different cases by scaling $s = 6$ and $s = 12$ of the highest element modes.

Independently of the number of element frequencies scaled, we demonstrate in Table IV that the lowest structural frequencies of the plate are not considerably affected. Observing the complete range of frequencies in Figure 13, we deduce that a mass scaling factor $\alpha = 10$ reduces the maximum frequency in the order of 2.5, speeding the computational cost for explicit dynamics more than 50%. However there exists a saturation limit in the scaling with this methodology, since a further increase of the scaling parameter, compare $\alpha = 10$ and $\alpha = 100$ in Figure 13, does not improve the benefit and will start to produce an ill-conditioning of the mass matrix.

Another important effect to observe in Figure 13 is the influence of the number of scaled element modes s on the frequencies. Increasing the number of scaled modes for a fixed α, does not affect the gain in the highest frequency but can degrade significantly the approximation in the mid frequency range. We conclude that we should use a minimum number of scaled modes to improve the accuracy.

Finally, it is important to mention that similar gains have been obtained by other scaling techniques proposed in the literature [22, 5]. But in these references, the mass scaling is made by augmentation of the RMM without discriminating higher and lower element modes. In fact, this separation has been found to be important in order to improve the approximation of the mid frequency range.

6. CONCLUSIONS

A new methodology for direct generation of the inverse mass matrix for discrete finite element equations of elastodynamics is presented, which is completely element-independent and does not require any special treatment of the elements adjacent to Dirichlet boundaries. In the present method,

the Dirichlet boundary conditions are handled by the method of localized Lagrange multipliers. This process is found to be computationally efficient, because matrices are sparse and only the factorization of a small matrix associated with the constrained DOFs is required. In structural dynamics, classical explicit time-integration methods equipped with a direct solver require an initial factorization of the mass matrix and the solution of a new free term every time step. If we choose Cholesky factorization for example, the total cost is around $\frac{1}{3}n^3$ flops plus $2n^2$ operations per time-step for each forward-backward substitution. With the proposed direct mass matrix inverse, factorization is not needed and operation count per time-step is reduced to a sparse-matrix vector multiplication with nm flops, where m is the average number of non-zero entries per row.

The proposed inverse mass-matrices have been tested for rod, beam, solid and shell elements, demonstrating excellent accuracy in terms of frequencies and time evolution of the DOFs obtained with explicit time-integration methods.

In addition, a new mass scaling technique is offered, which can be applied element-by-element and is frequency selective. Usage of scaled mass matrices reduces the maximum frequency of the system and thus increases the critical time step. Preliminary results demonstrate that the proposed selective mass scaling can attain reductions up to 40% in the highest frequencies without significantly affecting the low-mid frequency ranges. Further work along the line of the scaling technique will bring about a significant reduction of explicit transient analysis time. Work in this direction is underway.

REFERENCES

1. Hinton E, Rock T, Zienkiewicz OC. A note on mass lumping and related processes in the finite element method. *Earthquake Engineering & Structural Dynamics* 1976; **4**(3):245–9. doi: 10.1002/eqe.4290040305
2. Lombardo M, Askes H. Lumped mass finite element implementation of continuum theories with micro-inertia. *International Journal for Numerical Methods in Engineering* 2013; 96(7):448–466. doi: 10.1002/nme.4570
3. Hetherington J, Askes H. A mass matrix formulation for cohesive surface elements. *Theoretical and Applied Fracture Mechanics* 2014; 69:110–117. doi: 10.1016/j.tafmec.2013.11.011
4. Felippa CA, Guo Q, Park KC. Mass matrix templates: General description and 1D examples. *Archives of Computational Methods in Engineering* 2015; 22:1–65. doi: 10.1007/s11831-014-9108-x
5. Tkachuk A, Bischoff, M. Direct and sparse construction of consistent inverse mass matrices: general variational formulation and application to selective mass scaling. *International Journal for Numerical Methods in Engineering* 2015; 101:435-469. doi: 10.1002/nme.4805
6. Krenk S. Dispersion-corrected explicit integration of the wave equation. *Computer Methods in Applied Mechanics and Engineering* 2001; 191(8–10):975–987. doi: 10.1016/S0045-7825(01)00297-3
7. Gravouil A, Elguedj T, Maigre H. An explicit dynamics extended finite element method. Part 2: Element-by-element stable-explicit/explicit dynamic scheme. *Journal of Computational and Applied Mathematics* 2009; **198**:2318–2328. doi: 10.1016/j.cma.2009.02.018
8. Idesman A, Schmidt M, Foley J. Accurate finite element modeling of linear elastodynamics problems with the reduced dispersion error. *Computational Mechanics* 2011; 47(5):555–572. doi: 10.1007/s00466-010-0564-3
9. Park KC, Lim SJ, Huh H. A method for computation of discontinuous wave propagation in heterogeneous solids: basic algorithm description and application to one-dimensional problems. *International Journal for Numerical Methods in Engineering* 2012; **91**:622–643. doi: 10.1002/nme.4285
10. Cho SS, Park KC, Huh H. A method for multidimensional wave propagation analysis via component-wise partition of longitudinal and shear waves. *International Journal for Numerical Methods in Engineering* 2013; **95**:212–237. doi: 10.1002/nme.4495
11. Park KC, Felippa CA. A variational framework for solution method developments in structural mechanics. *Journal of Applied Mechanics* 1998; **65**(1):242–249. doi: 10.1115/1.2789032
12. Park KC, Felippa CA. A variational principle for the formulation of partitioned structural systems. *International Journal for Numerical Methods in Engineering* 2000; **47**:395–418. doi: 10.1002/(SICI)1097-0207(20000110/30)47:1/3%3C395::AID-NME777%3E3.0.CO;2-9

13. Park KC, Felippa CA, Gumaste UA. A localized Version of the method of Lagrange multipliers and its applications *Computational Mechanics* 2000, Volume: 24 Issue: 6 Pages: 476-490. doi: 10.1007/s004660050007

14. Gonzalez JA, Park KC, Felippa CA, Abascal R. A formulation based on localized Lagrange multipliers for BEM-FEM coupling in contact problems *Computer Methods in Applied Mechanics and Engineering* 2007, Volume: 197 Issue: 6-8 Pages: 623-640. doi: 10.1016/j.cma.2007.08.020

15. Wohlmuth B. A mortar finite element method using dual spaces for the Lagrange multiplier. *SIAM J. Numer. Anal.* 2000; **38**:989–1012. doi: 10.1137/S0036142999350929

16. Courant R, Friedrichs K, Lewy H. On the partial difference equations of mathematical physics. *IBM Journal of Research and Development* 1967; **11**(2):215–234. *English translation of the 1928 German original*, Courant R, Friedrichs K, Lewy H. Über die partiellen Differenzengleichungen der mathematischen Physik. doi: 10.1147/rd.112.0215

17. Macek RW, Aubert BH. A mass penalty technique to control the critical time increment in explicit dynamic finite element analyses. *Earthquake Engineering & Structural Dynamics* 1995; 24(10):1315–1331. doi: 10.1002/eqe.4290241003

18. Olovsson L, Unosson M, Simonsson K. Selective mass scaling for thin walled structures modeled with tri-linear solid elements. *Computational Mechanics* 2004; 34:134–136. doi: 10.1007/s00466-004-0560-6

19. Olovsson L, Simonsson K, Unosson M. Selective mass scaling for explicit finite element analyses. *International Journal for Numerical Methods in Engineering* 2005; 63(10):1436–1445. doi: 10.1002/nme.1293

20. Askes H, Nguyen D, Tyas A. Increasing the critical time step: micro-inertia, inertia penalties and mass scaling. *Computational Mechanics* 2011; 47:657–667. doi: 10.1007/s00466-010-0568-z

21. Cocchetti G, Pagani M, Perego U. Selective mass scaling and critical time-step estimate for explicit dynamics analyses with solid-shell elements. *Computers & Structures* 2013; 127:39–52. doi: 10.1016/j.compstruc.2012.10.021

22. Tkachuk A, Bischoff M. Variational methods for selective mass scaling. *Computational Mechanics* 2013; 52: 563–570. doi: 10.1007/s00466-013-0832-0

23. Tkachuk A, Bischoff M. Local and global strategies for optimal selective mass scaling. *Computational Mechanics* 2014; 53(6):1197–1207. doi: 10.1007/s00466-013-0961-5

24. Frias G, Aquino W, Pierson K, Heinstein M, Spencer B. A multiscale mass scaling approach for explicit time integration using proper orthogonal decomposition. *International Journal for Numerical Methods in Engineering* 2014; 97:799–818. doi: 10.1002/nme.4608

25. Park KC, Practical aspects of numerical time integration. *Computures & Structures* 1977; **7**:343–353. doi: 10.1016/0045-7949(77)90072-4

26. Hulbert G, Chung J. Explicit time integration algorithms for structural dynamics with optimal numerical dissipation. *Computer Methods in Applied Mechanics and Engineering* 1996; **137**:175–188. doi: 10.1016/S0045-7825(96)01036-5

27. Chang SY. An explicit method with improved stability property. *International Journal for Numerical Methods in Engineering* 2008; **77**(8):1100–1120. doi: 10.1002/nme.2452

28. Belytschko, T. and Liu, W.K. and Moran, B. and Elkhodary, K. *Nonlinear Finite Elements for Continua and Structures*. John Wiley & Sons, Ltd. 2014.

29. NAFEMS. The standard NAFEMS benchmarks. *National Agency for Finite Element Methods & Standards*. East Kilbride, Glasgow, U.K., 1990.